Asymmetric Vibrations and Chaos in Spherical Caps under Uniform Time-varying Pressure Fields

Giovanni Iarriccio (giovanni.iarriccio@unimore.it)
UNIMORE: Universita degli Studi di Modena e Reggio Emilia https://orcid.org/0000-0001-9323-8656
Antonio Zippo
UNIMORE: Universita degli Studi di Modena e Reggio Emilia
Francesco Pellicano
UNIMORE: Universita degli Studi di Modena e Reggio Emilia

Research Article

Keywords: Shells, spherical caps, vibrations, bifurcation, chaos

DOI: https://doi.org/10.21203/rs.3.rs-657063/v1

Asymmetric vibrations and chaos in spherical caps under uniform time-varying pressure fields

Iarriccio Giovanni

University of Modena and Reggio Emilia, 41121 Modena, Italy.

InterMech MoRe Centre, 41121 Modena, Italy.

ORCID id: 0000-0001-9323-8656

giovanni.iarriccio@unimore.it

Zippo Antonio

University of Modena and Reggio Emilia, 41121 Modena, Italy.

InterMech MoRe Centre, 41121 Modena, Italy.

ORCID id: 0000-0001-6206-2619

Pellicano Francesco

University of Modena and Reggio Emilia, 41121 Modena, Italy.

InterMech MoRe Centre, 41121 Modena, Italy.

ORCID id: 0000-0003-2465-6584

N. of pages: 32

N. of figures: 11

N. of tables: 1

Abstract

This paper presents a study on nonlinear asymmetric vibrations in shallow spherical caps under pressure loading. The Novozhilov's nonlinear shell theory is used for modelling the structural strains. A reduced-order model is developed through the Rayleigh-Ritz method and Lagrange equations. The equations of motion are numerically integrated using an implicit solver. The bifurcation scenario is addressed by varying the external excitation frequency. The occurrence of asymmetric vibrations related to quasi-periodic and chaotic motion is shown through the analysis of time histories, spectra, Poincaré maps, and phase planes.

Keywords

Shells, spherical caps, vibrations, bifurcation, chaos.

1. Introduction

Thin-walled structures like plates, panels, shells, and caps are important structural elements in Engineering; their applications can be found in Civil Engineering (roofs, vaults, tensile structures), Aerospace (airplanes, missiles and rockets); Mechanics (membrane based microsensors and energy harvesters).

These structures are strong and lightweight at the same time, but they are extremely sensitive to perturbations, present a complicated instability behaviors and are very difficult to model. They could buckle under the action of critical loads, following sub-critical post-buckling paths; moreover, they can exhibit non-linear dynamic phenomena, such as chaotic vibrations, when the amplitude of vibration is moderately large.

Nowadays, many theories and simplified models are available for studying shell systems, even in the presence of fluid-structure interaction or thermal fields. Nevertheless, new challenges come from the new frontiers of the Engineering, which asks for even more reliable models where complicating effects are taken into account for exploiting the nonlinearities: for example, phenomena such as multi-stability or the pull-in, can be desired features through which designers can achieve structural optimization and develop high performance devices.

A short literature review is reported here for introducing the reader to the most important and recent scientific contributions to the study of thin walled structures, with a specific focus to spherical caps dynamics.

Concerning the elastic stability of shells, buckling problems are classified into: Static buckling when loads are applied extremely slowly; Dynamic buckling when the loads are suddenly applied (step loads).

From a literature review, there is a discrepancy between experimental data and theoretical results. The primary sources of inconsistencies, that lead to an experimental lower buckling load than the one theoretically predicted, are (i) the high sensitivity of shells to geometric imperfections and non-uniform material distribution, and (ii) the post-buckling behavior is strongly affected by nonlinearities.

Let us first focus on the static instability of the spherical caps under an external pressure load. Krenze and Kiernan [1] showed the importance of producing high quality specimens for performing experimental tests. In the same period, Huang

[2] and Weinitsche [3] used Margurre's theory with possibility of having non-symmetric buckling. They showed how, for deeper caps, the wavelength of the buckling modes was higher compared to shallow caps, and numerical results agreed with the experimental ones available at that time. These results were experimentally confirmed by Yamada et al. [4] two decades later.

The role of geometric imperfections on critical static loads of caps was investigated in Refs. [5,6]. Results pointed out how the shape of the geometric imperfection affects the decrement of the critical buckling load; often the snap-through phenomenon disappeared due to imperfections, and continuous and stable buckling paths were shown by the pressure-deflection diagrams.

Since the measurement of imperfections it is not always possible for large scale applications, NASA proposed an empirical formula based on the lower envelope of a series of experimental data [7]. Nowadays, the specimens quality is higher and other techniques have been proposed for improving the NASA empirical formula[8,9].

A further reduction of the load-carrying capacity can be observed when the time dependency of the load is considered, i.e. in the case of dynamic buckling.

Lock et al. [10] experimentally analyzed the buckling of shallow domes under a pressure-step loading. They discussed the difference between "direct" and "indirect" snapping phenomena. The direct snapping is a catastrophic phenomenon and involves only symmetric vibrations; conversely, the indirect snapping occurs after a transient and the contribution of the non-symmetric modes is not negligible after the snapping.

Stricklin et al. [11] used nonlinear Novozhilov's theory for investigating the static stresses in shells of revolution and improved their model for studying the dynamic buckling in Ref. [12]. The equilibrium equations were obtained through Castigliano's theorem. Numerical results were compared with experimental ones, and an excellent agreement was proved. The dynamic model was derived employing of the Lagrange equations by considering only axisymmetric modes, and the results confirmed the previous analyses [13,14].

Ball and Burt [15] numerically investigated the dynamic buckling of clamped shallow spherical caps under symmetric and nearly-symmetric step pressure loads. Asymmetric modes were considered, and the buckling load of geometrically perfect structures of different shallowness was given.

The asymmetric dynamic buckling of shallow spherical caps was investigated even by Akkas [16], who showed that the asymmetric buckling under step pressure load results in cusps in phase-plane diagrams.

Further results concerning the dynamic buckling of imperfect caps can be found in Refs. [17–19], where the possibility of having plastic deformations was considered as well.

In the framework of spherical caps under harmonic loads, the literature is not as vast as for the buckling. Reasons must be sought in the fact that: (i) spherical caps are a particular case of doubly curved shells, they are modeled through equations that are more complex with respect to plates and cylindrical shells; (ii) the high computational cost related to the numerical integration of the equations of motion limited for long time the analysis to low dimensional models and axisymmetric vibrations.

Using a theory proposed by Yu [20], Grossman et al. [21] investigated the axisymmetric nonlinear vibrations of shallow spherical caps with different boundary conditions. This study compared flat plates to curved caps, and the results pointed out the transition from hardening to softening nonlinearity when the surface curvature is increased.

Evensen and Iwanovsky [22] were the first to perform both analytically and experimental analyses on shallow spherical caps under a combination of static and sinusoidal external pressure loads. The analytical model was based on the Marguerre's nonlinear shell theory. Axisymmetric deflections and uniform load distribution were considered. A detailed scheme of the experimental setup was reported and discussed. Numerical results concerning free vibrations were in excellent agreement with experiments. Unfortunately, differences were shown in several nonlinear forced cases. Such discrepancies were mainly attributed to the interaction between static and dynamic loads, and to the asymmetric vibrations observed during the experiments.

Yasuda and Kushida [23] studied the forced vibration of caps under harmonic point loads. The activation of subharmonic motion due to internal resonances was observed. In order to validate the numerical model, experiments were performed on a bent circular plate clamped at its edges. The structure was loaded by a concentrated force induced by two electric magnets, and experimental results agreed with the numerical ones.

The axisymmetric vibrations of pre-loaded shallow spherical caps were investigated by Gonçalves [24,25] and Soliman and Gonçalves [26]. For obtaining a reduced-order model (ROM), the Galerkin method was considered. The displacement fields were expanded by using the Bessel functions, and the resulting equations of motion were solved through the Newton-Rapson method. Results showed a strong influence of geometric imperfections and their spatial shape. Softening nonlinearity can be turned to hardening by imposing a suitable initial imperfection of a given shape and amplitude, as shown by the reported backbone curves. Moreover, assuming the excitation frequency as a control parameter, the bifurcation analysis pointed out the existence of period-doubling cascades and chaotic oscillations. The onset of such phenomena is due to energy given by the harmonic pressure to the shell, which leads to multiple back-and-forth jumps between potential wells.

Thomas et al. [27,28] studied the response of a free-edge shallow spherical cap under harmonic excitation. Using the multiple-scale perturbation method, results showed that, having integer or quasi-integer ratio between natural frequencies is not a sufficient condition for having internal resonances activation. This is due to the body symmetry, which leads to the canceling of some nonlinear coefficient in the ODEs. Experiments were carried out by forcing the specimen using an electromagnetic coil. The occurrence of an internal resonance between two conjugate asymmetric modes and one axisymmetric mode (1:1:2) was proven, a good qualitative fitting between theory and experiments was shown for small forcing amplitude.

Touzè et al.[29,30] used the nonlinear normal modes approach (NNMs) for predicting the trend of nonlinearity for each mode as a function of the spherical cap geometric aspect ratios. In particular, the transition from hardening to softening nonlinearity was addressed.

Chaotic vibrations in shallow shells with circular planform were investigated by Krysko et al. [31]: the role of size-dependent parameters on vibrations of nano shells were analyzed. The system of PDE was reduced using a finite difference method (FDM), and the resulting system was solved through a Runge-Kutta scheme. By comparing Fourier's spectra, Poincaré maps, Lyapunov exponents, and Morlet wavelet, the authors showed that, considering the size-effect shells

exhibit regular vibrations whereas with the same load conditions neglecting the size-effect one obtains chaotic vibrations.

The present work aims to address to some questions arisen recently in Ref.[32] on pressure loaded spherical caps, where the limits of axisymmetric models were shown using continuation techniques. Here the Novozhilov's geometrically nonlinear theory is considered. For the analysis of the linearized equations, the Rayleigh-Ritz approach is considered to obtain the mode shapes in a semi-analytical way. Lagrange equations are used for reducing the system of nonlinear partial differential equations, PDEs, to a system of ordinary differential equations, ODEs. A bifurcation analysis of is carried out by directly integrating the equations of motion. Results are presented and discussed with the help of bifurcation diagrams and other useful tools, such as Poincaré maps and Fourier's spectra. The superimposition of a static and a dynamic pressure yields to non-periodic and chaotic oscillation related to the activation of asymmetric modes.

2. Problem Formulation

A spherical cap having radius R, base radius a, cap height s, and thickness h, is considered, see Fig. 1(a-c). A spherical coordinate system $(O;\varphi,\vartheta,z)$ is centered at the top of the cap O. The curvilinear coordinates (φ,ϑ) identify a point P of the shell middle surface, z is the radial distance of a generic point of the shell from the middle surface. Three displacement fields, meridional $u(\eta,\vartheta,t)$, circumferential $v(\eta,\vartheta,t)$, and radial $w(\eta,\vartheta,t)$, describe the deformed configuration of the middle surface; t is the time variable.

Limiting the analysis to shallow spherical caps, the Lamé parameters of the undeformed middle surface are $A_1 = R$ and $A_2 \cong \varphi_b \cdot \eta$; where $\eta = \varphi/\varphi_B$ is the meridional non-dimensional coordinate.

For describing the relationships between strains and displacements, the Novozhilov's nonlinear shell theory [33] is considered. Such theory is based on the Kirchhoff-Love hypothesis, which states that: (i) the shell is thin $h \ll R$ and $h \ll a$, (ii) strains, (iii) transverse normal stresses are small, and (iv) the normal to the undeformed middle surface remains normal after deformation, and no

thickness stretching occurs. The hypothesis of small displacements is relaxed in the nonlinear analysis.

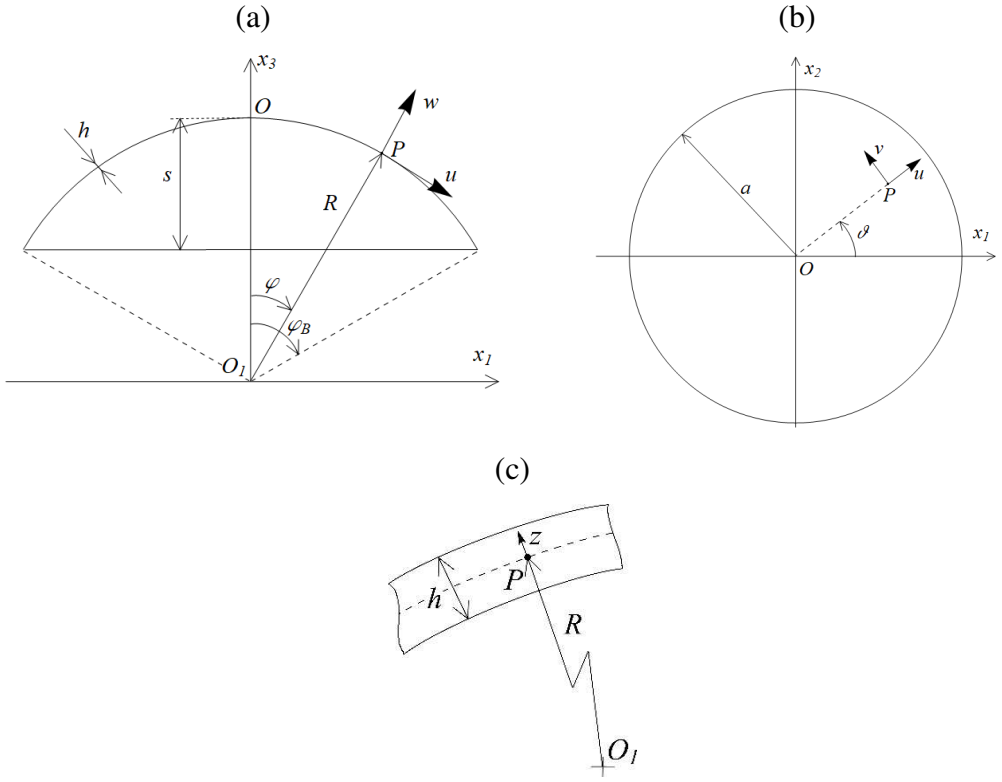

Fig. 1. Spherical cap geometry and coordinate system: (a) cross-section view, (b) top view, and (c) breakout-section view.

Because of the aforementioned hypothesis, the strains $\hat{\varepsilon}_i, \hat{\gamma}_{ij}$ at an arbitrary point of the cap linearly vary along the thickness; moreover, the plane-stress hypothesis is considered. The strains are given by:

$$\hat{\varepsilon}_\eta = \varepsilon_\eta + z \cdot k_\eta, \tag{1.a}$$

$$\hat{\varepsilon}_\vartheta = \varepsilon_\vartheta + z \cdot k_\vartheta, \tag{1.b}$$

$$\hat{\gamma}_{\eta\vartheta} = \gamma_{\eta\vartheta} + z \cdot k_{\eta\vartheta}, \tag{1.c}$$

where ε_η, ε_ϑ, $\gamma_{\eta\vartheta}$ are the middle surface strains, k_η, k_ϑ, and $k_{\eta\vartheta}$ are the changes in curvatures and torsion of the middle surface of the shell, which depend on the middle surface displacement fields through the following relationships:

$$\varepsilon_\eta = e_{11} + \frac{1}{2}\left(e_{11}^2 + e_{12}^2 + e_{13}^2\right), \tag{2.a}$$

$$\varepsilon_\vartheta = e_{22} + \frac{1}{2}\left(e_{21}^2 + e_{22}^2 + e_{23}^2\right), \tag{2.b}$$

$$\gamma_{\eta\vartheta} = e_{12} + e_{21} + e_{11}e_{21} + e_{12}e_{22} + e_{12}e_{23}, \tag{2.c}$$

$$k_\eta = -\frac{1}{A_1}\frac{\partial e_{13}}{\varphi_b \partial \eta} + \frac{e_{11} + e_{22}}{R}, \tag{2.d}$$

$$k_\vartheta = -\frac{1}{A_1 A_2}\frac{\partial A_2}{\varphi_b \partial \eta} e_{13} + \frac{1}{A_1}\frac{\partial e_{23}}{\varphi_b \partial \eta} + \frac{e_{11} + e_{22}}{R}, \tag{2.e}$$

$$k_{\eta\vartheta} = -\frac{1}{A_2}\frac{\partial e_{13}}{\partial \vartheta} - \frac{1}{A_1}\frac{\partial e_{23}}{\varphi_b \partial \eta} + \frac{1}{A_1 A_2}\frac{\partial A_2}{\varphi_b \partial \eta} e_{23}. \tag{2.f}$$

221

222 where the strain components e_{ij} are:

223

$$e_{11} = \frac{1}{A_1}\frac{\partial u}{\varphi_b \partial \eta} + \frac{w}{R}, \tag{3.a}$$

$$e_{12} = \frac{1}{A_2}\frac{\partial u}{\partial \vartheta} - \frac{1}{A_1 A_2}\frac{\partial A_2}{\varphi_b \partial \eta} v, \tag{3.b}$$

$$e_{13} = -\frac{u}{R} + \frac{1}{A_1}\frac{\partial w}{\varphi_b \partial \eta}, \tag{3.c}$$

$$e_{21} = \frac{1}{A_1}\frac{\partial v}{\varphi_b \partial \eta}, \tag{3.d}$$

$$e_{22} = \frac{1}{A_1 A_2}\frac{\partial A_2}{\varphi_b \partial \eta} u + \frac{1}{A_2}\frac{\partial v}{\partial \vartheta} + \frac{w}{R}, \tag{3.e}$$

$$e_{23} = -\frac{v}{R} + \frac{1}{A_2}\frac{\partial w}{\partial \vartheta}. \tag{3.f}$$

224

225 Considering an elastic linear, homogeneous and isotropic continuum, one can use
226 the Hooke's law, i.e. the following stress-strain relationships:

227

$$\begin{pmatrix} \hat{\sigma}_\eta \\ \hat{\sigma}_\vartheta \\ \hat{\tau}_{\eta\vartheta} \end{pmatrix} = \begin{bmatrix} \frac{E}{1-\nu^2} & \frac{\nu E}{1-\nu^2} & 0 \\ \frac{\nu E}{1-\nu^2} & \frac{E}{1-\nu^2} & 0 \\ 0 & 0 & \frac{E}{2(1+\nu)} \end{bmatrix} \begin{pmatrix} \hat{\varepsilon}_\eta \\ \hat{\varepsilon}_\vartheta \\ \hat{\gamma}_{\eta\vartheta} \end{pmatrix} \tag{4.a}$$

where E and ν are the Young's modulus and the Poisson's ratio, respectively. By considering the strains (1.a-d) and the stresses (4.a-b), the elastic strain energy U_S [34] of a thin shallow spherical cap is given by

$$\begin{aligned} U_S &= \frac{1}{2}\int_{-h/2}^{h/2}\int_{\eta_0}^{1}\int_{0}^{2\pi}\left(\hat{\sigma}_\eta\hat{\varepsilon}_\eta + \hat{\sigma}_\vartheta\hat{\varepsilon}_\vartheta + \hat{\tau}_{\eta\vartheta}\hat{\gamma}_{\eta\vartheta}\right)A_1A_2\varphi_b\,d\vartheta\,d\eta \\ &= \frac{1}{2}\frac{Eh}{1-\nu^2}\int_{\eta_0}^{1}\int_{0}^{2\pi}\left(\varepsilon_\eta^2 + \varepsilon_\vartheta^2 + 2\nu\varepsilon_\eta\varepsilon_\vartheta + \frac{1-\nu}{2}\gamma_{\eta\vartheta}^2\right)A_1A_2\varphi_b\,d\vartheta\,d\eta + \\ &\quad \frac{1}{2}\frac{Eh^3}{12(1-\nu^2)}\int_{\eta_0}^{1}\int_{0}^{2\pi}\left(k_\eta^2 + k_\vartheta^2 + 2\nu k_\eta k_\vartheta + \frac{1-\nu}{2}k_{\eta\vartheta}^2\right)A_1A_2\varphi_b\,d\vartheta\,d\eta \end{aligned} \tag{5}$$

while, the kinetic energy T_S, under the hypothesis of negligible rotary inertia [34], is given by

$$T_S = \frac{1}{2}\rho_S h\int_{\eta_0}^{1}\int_{0}^{2\pi}\left(\dot{u}^2 + \dot{v}^2 + \dot{w}^2\right)A_1A_2\varphi_b\,d\vartheta\,d\eta \tag{6}$$

where ρ_S is the material mass density, η_0 is the half opening angle of a hole assumed a the cap pole for avoiding the singularity due to the spherical reference system [35].

2.1. Approximate eigenfunctions

In order to develop a ROM for studying the cap nonlinear dynamics, in this section the eigenfunctions of the linearized operator are obtained through the Rayleigh-Ritz approach [36].

In the present study, clamped boundary conditions are considered at the circular edge

$$u = v = w = \frac{\partial w}{\partial \eta} = 0 \quad for \quad \eta = 1 \tag{7}$$

while, no boundary conditions are considered at the cap pole.

The Rayleigh-Ritz approach requires that a trial function set respects the geometric boundary conditions only [37]; on the other hand, the stress-free boundary conditions at the cap pole (where the small hole is present) are neglected.

The generic mode of vibration can be described by considering three displacement fields $u(\eta,\vartheta,t), v(\eta,\vartheta,t),$ and $w(\eta,\vartheta,t)$, which obey to the same time law $f(t)$, i.e. the variable separation can be considered:

$$u(\eta,\vartheta,t) = U(\eta,\vartheta)\cdot f(t), \tag{8.a}$$

$$v(\eta,\vartheta,t) = V(\eta,\vartheta)\cdot f(t), \tag{8.b}$$

$$w(\eta,\vartheta,t) = W(\eta,\vartheta)\cdot f(t). \tag{8.c}$$

$U(\eta,\vartheta), V(\eta,\vartheta),$ and $W(\eta,\vartheta)$ are spatial functions denoting the mode shapes i.e. eigenfunctions.

The eigenfunctions are now discretized using a linear combination of functions. Legendre polynomials are considered in the meridional direction and trigonometric functions are assumed in the circular direction.

$$U(\eta,\vartheta) = \sum_{m=0}^{M_u}\sum_{n=0}^{N} \tilde{U}_{m,n} P_m^{*}(\eta)\cos(n\vartheta), \tag{9.a}$$

$$V(\eta,\vartheta) = \sum_{m=0}^{M_v} \tilde{V}_{m,0} P_m^{*}(\eta) + \sum_{m=0}^{M_v}\sum_{n=1}^{N} \tilde{V}_{m,n} P_m^{*}(\eta)\sin(n\vartheta), \tag{9.b}$$

$$W(\eta,\vartheta) = \sum_{m=0}^{M_w}\sum_{n=0}^{N} \tilde{W}_{m,n} P_m^{*}(\eta)\cos(n\vartheta). \tag{9.c}$$

where $P_m^*(\eta) = P_m(2\eta - 1)$ is the m-th Legendre polynomial of the first kind shifted in the domain $\eta \in [0,1]$; m is related to the number of meridional wavelength; n is the number of nodal diameters.

Because of the axial symmetry, spherical caps exhibit conjugate modes, called driven and companion mode shapes or conjugate modes [38,39]. These modes have the same natural frequency and shape, but the displacement fields are angularly shifted of $\pi/2n$. Conjugate modes describe standing waves, but circumferential travelling waves could arise when nonlinear mode coupling occurs [40–42]. Therefore, companion modes should be considered when a nonlinear analysis is carried out.

$$U(\eta,\vartheta) = \sum_{m=0}^{M_u} \sum_{n=1}^{N} \tilde{U}_{m,n} P_m^*(\eta) \sin(n\vartheta), \tag{10.a}$$

$$V(\eta,\vartheta) = \sum_{m=0}^{M_v} \sum_{n=1}^{N} \tilde{V}_{m,n} P_m^*(\eta) \cos(n\vartheta), \tag{10.b}$$

$$W(\eta,\vartheta) = \sum_{m=0}^{M_w} \sum_{n=1}^{N} \tilde{W}_{m,n} P_m^*(\eta) \sin(n\vartheta). \tag{10.c}$$

It is worth noting that asymmetric modes are not associated to multiple eigenvalues, therefore, they have not companion modes.

By imposing the set of boundary conditions (7) to the discretized eigenfunctions, a system of algebraic equations is obtained:

$$\sum_{m=0}^{M_u} \tilde{U}_{m,n} P_m^*(\eta) = 0, \tag{12.a}$$

$$\sum_{m=0}^{M_v} \tilde{V}_{m,n} P_m^*(\eta) = 0, \tag{12.b}$$

$$\sum_{m=0}^{M_w} \tilde{W}_{m,n} P_m^*(\eta) = 0, \quad \textit{for} \quad \eta=1 \tag{12.c}$$

$$\sum_{m=0}^{M_w} \tilde{W}_{m,n} \frac{\partial}{\partial \eta} P_m^*(\eta) = 0, \tag{12.d}$$

The solution of this linear system allows to express $(\tilde{U}_{0,n}, \tilde{V}_{0,n}, \tilde{W}_{0,n}, \tilde{W}_{1,n})$ in terms of the remaining coefficients $(\tilde{U}_{m,n}, \tilde{V}_{m,n}, \tilde{W}_{m,n})$; the latter coefficients can be

reordered in a vector $\tilde{\mathbf{q}}$ [43] with a number of elements equal to $N_{max} = (M_u + M_v + M_w + 3 - b)(N+1)$, where *b=4* for a clamped circular cap [32]. Considering only the linear terms in the strain-displacement relations (2.a-f), the eigenvalue problem for approximating the natural frequencies and mode shapes of the structure is obtained by imposing the stationarity of the Rayleigh's quotient $R(\tilde{\mathbf{q}}) = U_S(\tilde{\mathbf{q}}) / T_S^*(\tilde{\mathbf{q}})$, where $U_S(\tilde{\mathbf{q}})$ is the maximum potential energy during a "modal" oscillation, and $T_S^*(\tilde{\mathbf{q}}) = T_S(\tilde{\mathbf{q}}) / \omega^2$.

$$(-\omega^2 \mathbf{M} + \mathbf{K})\tilde{\mathbf{q}} = \mathbf{0}. \tag{13}$$

ω is the circular frequency of the harmonic motion; $\mathbf{M}$ and $\mathbf{K}$ are the mass matrix and the stiffness matrix of the discrete linearized system, respectively.

The *i*-th solution of equation (13), $\left(\omega^{(i)}, \tilde{\mathbf{q}}^{(i)}\right)$, gives the approximation of the *i*-th natural frequency and mode shape, respectively.

To improve the results readability and the numerical accuracy, the approximated mode shapes are normalized using the approach of Ref.[43], and the following condition is sought $\max\left[\text{abs}\left[U^{(i)}(\eta,\vartheta)\right], \text{abs}\left[V^{(i)}(\eta,\vartheta)\right], \text{abs}\left[W^{(i)}(\eta,\vartheta)\right]\right] = 1$.

2.2 Nonlinear vibrations

Synchronous motion and small amplitude displacement hypotheses are now relaxed, as well as the absence of external excitation.

In such conditions we cannot claim anymore that the vibration is harmonic or periodic.

The approach used for analyzing the nonlinear dynamics of the cap is based on the spectral theorem, i.e., taking advantage from the completeness of the eigenfunctions calculated on the previous section, the displacement fields are expanded as follows:

$$u(\eta,\vartheta,t) = \sum_i^{M_{u,1}} \sum_j^{N_u} [U_{i,j}^{(d)}(\eta,\vartheta) f_{u,i,j}^{(d)}(t) + U_{i,j}^{(c)}(\eta,\vartheta) f_{u,i,j}^{(c)}(t)] \tag{14.a}$$

$$v(\eta,\vartheta,t) = \sum_i^{M_{v,1}} \sum_j^{N_v} [V_{i,j}^{(d)}(\eta,\vartheta) f_{v,i,j}^{(d)}(t) + V_{i,j}^{(c)}(\eta,\vartheta) f_{v,i,j}^{(c)}(t)] \tag{14.b}$$

$$w(\eta,\vartheta,t)=\sum_i^{M_{w,1}}\sum_j^{N_w}[W_{i,j}^{(d)}(\eta,\vartheta)f_{w,i,j}^{(d)}(t)+W_{i,j}^{(c)}(\eta,\vartheta)f_{w,i,j}^{(c)}(t)] \quad (14.c)$$

where *d* and *c* are related to the driven and companion modes, respectively; *i* and *j* identify the number of meridional and circumferential wavelengths; $f_{k,i,j}^{(\cdot)}$ are the time dependent unknown generalized coordinates.

For thin-walled bodies under external pressure load, two assumptions are common in the literature: (i) the pressure is considered as a radial non-follower load; (ii) the load distribution is applied to the middle surface [33].

The former approximation simplifies the numerical calculations and reduces the numerical effort; however, it could underestimate the safety factor in structures that undergo to large deflections. The latter assumption is a valid approximation for thin shells and should be removed for thicker structures.

Considering a configuration-dependent pressure distribution that always acts orthogonal to the surface (follower force distribution), the expression of the *j*-th generalized force is given by Amabili and Breslavsky, where only the linear strain terms are retained [44]

$$\frac{\partial W_p}{\partial q_j}\cong\int_{\eta_0}^{1}\int_0^{2\pi}p(t)\left[-\frac{\partial u}{\partial q_j}e_{12}-\frac{\partial v}{\partial q_j}e_{23}+-\frac{\partial w}{\partial q_j}(1+e_{11}+e_{22})\right]A_1A_2\varphi_b d\vartheta d\eta, \quad (15)$$

The external pressure consists of a static and a dynamic component $p(t)=p_s+p_d\cos(\Omega t)$ is the external pressure. The pressure is positive when inflates the structure.

Taking into account the full expression of the strains (2.a-f) and replacing them into the energies and virtual work formulae, the equations of motion are derived by the Lagrange equations

$$\frac{d}{dt}\left(\frac{\partial T_S}{\partial\dot{q}_j}\right)+\frac{\partial U_S}{\partial q_j}=\frac{\partial W_p}{\partial q_j},\quad for\quad j=1,2,...,N_{dofs} \quad (16)$$

N_{dofs} indicates the number of degrees of freedom of the nonlinear ODEs. Such set could be rewritten into state-space form.

The set of nonlinear ODEs could be rewritten into the following first-order form:

340

$$\begin{cases} \dot{\mathbf{q}} = \mathbf{y} \\ \dot{\mathbf{y}} = \mathbf{M}^{-1}[-\mathbf{C}\mathbf{y} - \mathbf{K}_{NL}\mathbf{q} + \mathbf{p}_s + \mathbf{p}_d \cos(\Omega t)] \end{cases} \quad (17)$$

341

342 Note that $\mathbf{M}^{-1}\mathbf{C} = \text{diag}(2\zeta_j\omega_j)$, where ζ_j and ω_j are the damping ration and the
343 natural frequencies of the j^{th} generalized coordinate; $\mathbf{p}_s$ and $\mathbf{p}_d$ are the
344 generalized force vectors due to the static and dynamic pressure, respectively; Ω
345 is the frequency of the external excitation; $\mathbf{y}$ is the generalized velocity vector.
346 In the following analysis, the equations of motion are reduced to a
347 nondimensional form: the amplitudes are divided by the shell thickness; the time
348 is divided by the period of the first axisymmetric resonant mode.
349

$$\hat{\mathbf{q}} = \mathbf{q}/h \qquad \tau = \omega_{1,0} \cdot t \quad (18)$$

350

351 The pressure is normalized through to the Zoelly's critical buckling pressure of a
352 complete, isotropic, and homogeneous sphere, see Ref. [45]
353

$$p_{cr} = \frac{2E}{\sqrt{3\left(1-\nu^2\right)}}\left(\frac{h}{R}\right)^2 \quad (19)$$

354

355 For the sake of completeness, the expression of the parameter λ is here reported
356 due to its important meaning: λ includes information on the thinness and the
357 shallowness of the investigated structure.
358

$$\lambda = \sqrt[4]{12(1-\nu^2)} \cdot \frac{a}{\sqrt{Rh}}, \quad (20)$$

359

360 3. Numerical Results

361 Consider a clamped shallow spherical cap, having a uniform thickness, made of
362 steel. Using the 38 *dofs* nonlinear model developed in Ref [32], the nonlinear
363 dynamic response of the cap under a time-varying harmonic pressure is

investigated. For the sake of clarity, the linear mode shapes retained into the nonlinear ROM are listed in Table 1:it must be noted that both driven and companion vibration modes have been included for the asymmetric mode shapes (*n=0*).

Table 1 – Normalized natural frequencies and mode shapes considered into the nonlinear reduced-order model [32].

$\omega_{m,n}/\omega_{1,0}$	***m***	***n***	***Modal displacement field***
1.0000	*1*	*0*	*w,u*
1.1052	*1*	*2*	*w,v,u*
1.3030	*2*	*0*	*w,u*
1.6838	*1*	*4*	*v*
1.9650	*2*	*2*	*w,v,u*
2.0695	*3*	*0*	*w,u*
2.4869	*2*	*4*	*v*
2.6661	*3*	*2*	*w,v,u*
3.4519	*4*	*0*	*w,u*
4.1146	*3*	*4*	*v*
5.3040	*5*	*0*	*w,u*
7.3148	*4*	*4*	*v*
7.7524	*6*	*0*	*w,u*

The geometrical and structural data are listed as follows: $R = 0.8\ m$, $h = R/300$, $a = 0.152\ m$, $s = 0.0147\ m$, $\varphi_b = 11.0\deg$, $E = 200 \cdot 10^9\ Pa$, $\rho = 7800\ kg/m^3$, $\nu = 0.3$, $\lambda = 6$. The natural frequency of the first axisymmetric mode, $\omega_{1,0}$, is considered for the time nondimensionalization, as already stated in (18), and a modal damping factor $\varsigma_j = 0.012,\ j = 1,2,...N_{dofs}$ is assumed.

A static pressure load $p_s = -0.40 \cdot p_{cr}$ (lower than the critical buckling pressure) acts on the shell while a dynamic component, of amplitude $p_d = 0.020 \cdot p_{cr}$, is superimposed to the static one.

The set of nonlinear ODEs (17) is numerically solved by using the Fortran routine for time integration RADAU5 [46]. This integrator was developed for solving stiff ODEs and is based on the implicit Runge-Kutta method of order 5, 3-stages, with

step-size control. To carry out the bifurcation analysis, the excitation frequency is varied forward and backward in the frequency range $\Omega/\omega_{1,0} \in [1.07400, 1.10500]$, where the occurrence of dynamic instabilities were proven through a path-following analysis in Ref. [32].

The parameters used for setting the time-response analysis are the following: 125 excitation frequency steps with a step-size of $\Delta\Omega/\omega_{1,0} = \pm 0.00025$; a sampling frequency equal to 40 times the excitation frequency; 600 excitation periods of integration, where only 300 periods are retained for getting rid of the transient response. When the simulation starts, homogeneous initial conditions are considered, then, for further steps (different frequencies), the initial conditions are assumed to be the final state of the previous step, with a perturbation of amplitude 0.01 (dimensionless) applied to every generalized coordinate. For the frequencies where the system is sensitive to small perturbations and prone to exhibits chaotic motion, the perturbation allows the system to leave an almost unstable orbit and find remote attractors.

In Fig. 2(a,b), the frequency-response curves obtained by directly integrating the ODEs are compared to continuation method results [32]. Starting from $\Omega/\omega_{1,0} = 1.0740$ and considering an increasing forcing frequency (red asterisks), $f_{w,1,0}$ follows the stable solution path 1 (continuous black line) and switch on branch 2 after the period-doubling (PD) at $\Omega/\omega_{1,0} = 1.08275$, see Fig. 2(a), where the bifurcation leads to the onset of asymmetric oscillations, see Fig. 2(b). Large amplitude vibrations, with a discontinuous amplitude variation, occur for $\Omega/\omega_{1,0} \in [1.08425, 1.09375]$, where the path following analysis pointed out the coexistence of multiple unstable solution (dotted black line), i.e. one or more Floquet multipliers fall outside the unit circle. By considering $\Omega/\omega_{1,0} > 1.09500$, $f_{w,1,0}$ lies again on a stable periodic solution, while $f_{w,1,2}^{(d)}$ follows a branch not shown in Ref. [32] and asymmetric oscillations persists until a second PD bifurcation at $\Omega/\omega_{1,0} = 1.10125$.

Considering now a backward frequency variation (blue circles), the frequency-response curve trend is almost the same obtained by considering an upward frequency variation. However, when the harmonic pressure acts on the structure with a frequency $\Omega/\omega_{1,0} \in [1.07650, 1.08400]$, both the coordinates $f_{w,1,0}$ and $f_{w,1,2}^{(d)}$

follows secondary solution branches not shown by the path following analysis [32]. A further reduction of the forcing frequency, leads to a sudden response jump that restores a purely axisymmetric overall motion of the cap.

(a)

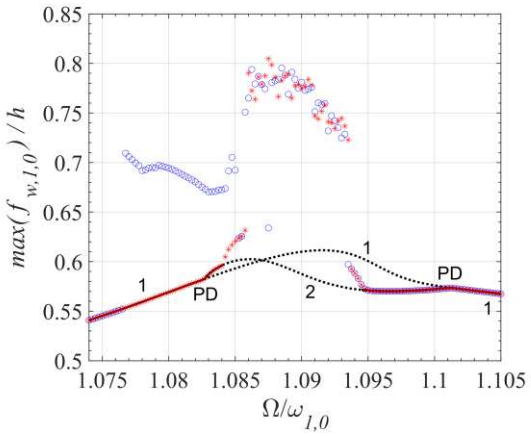

(b)

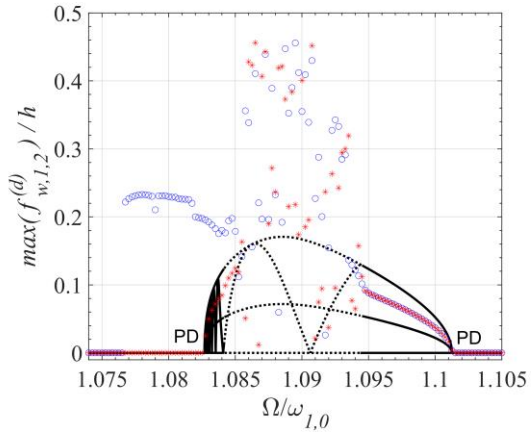

Fig. 2. Frequency-response curves: (a) first axisymmetric mode, (b) driven asymmetric mode (1,2). (- Ref.[32], * **upward frequency variation,** ○ **downward frequency variation, "PD" period-doubling).**

In order to provide further information for understanding the path-following analysis results, bifurcation diagrams of the Poincaré maps are here presented and discussed.

In Fig. 3(a-d), the bifurcation diagrams obtained for an increasing excitation frequency are shown. The response is fully axisymmetric until $\Omega/\omega_{1,0}=1.08275$, where the activation of the asymmetric conjugate modes $f_{w,1,2}^{(d)}$ and $f_{w,1,2}^{(c)}$ is governed by 2-T subharmonic responses, see Fig. 3(c,d), although the axisymmetric generalized coordinates $f_{w,1,0}$ and $f_{w,2,0}$ retain 1-T periodic oscillations, Fig. 3(a, b). Nonperiodic vibrations arise for $\Omega/\omega_{1,0}=1.08425$, where a Neimark-Sacker bifurcation leads to amplitude-modulated oscillations. For $\Omega/\omega_{1,0}=1.08600$, the quasi-periodic response collapse on a chaotic attractor. Chaotic region holds until $\Omega/\omega_{1,0}=1.94250$, where quasi-periodic motion is restored and the conjugated asymmetric coordinates $f_{w,1,2}^{(d)}$ and $f_{w,1,2}^{(c)}$ display 2-T periodic oscillations. An additional excitation frequency increment gives rise to a period-doubling bifurcation at $\Omega/\omega_{1,0}=1.10125$, in agreement with the finding of [32]. Beyond the period doubling, the response becomes periodic with the same frequency of the excitation and the contribution of the asymmetric modes on the overall oscillation becomes null, as already pointed out form the analysis of the frequency-response diagrams in Fig. 2(a,b).

Bifurcation diagrams of the Poincaré sections are now analyzed by considering a decreasing excitation frequency, Fig. 4(a-d).

Starting from $\Omega/\omega_{1,0}=1.10500$, the structural response undergoes sequentially to a period-doubling bifurcation at $\Omega/\omega_{1,0}=1.10125$ and a Neimark-Sacker bifurcation at $\Omega/\omega_{1,0}=1.09450$. The amplitude-modulated oscillations burst into a chaotic attractor at $\Omega/\omega_{1,0}=1.09325$. Inside the range $\Omega/\omega_{1,0}\in[1.08500,1.09325]$, the response jumps from chaotic to quasi-periodic attractors. A further reduction of the control parameter leads to a complex dynamic behavior, where the solution alternates quasi-periodic to 5T-subharmonic vibrations. Then, when $\Omega/\omega_{1,0}<1.07650$, only axisymmetric states exist.

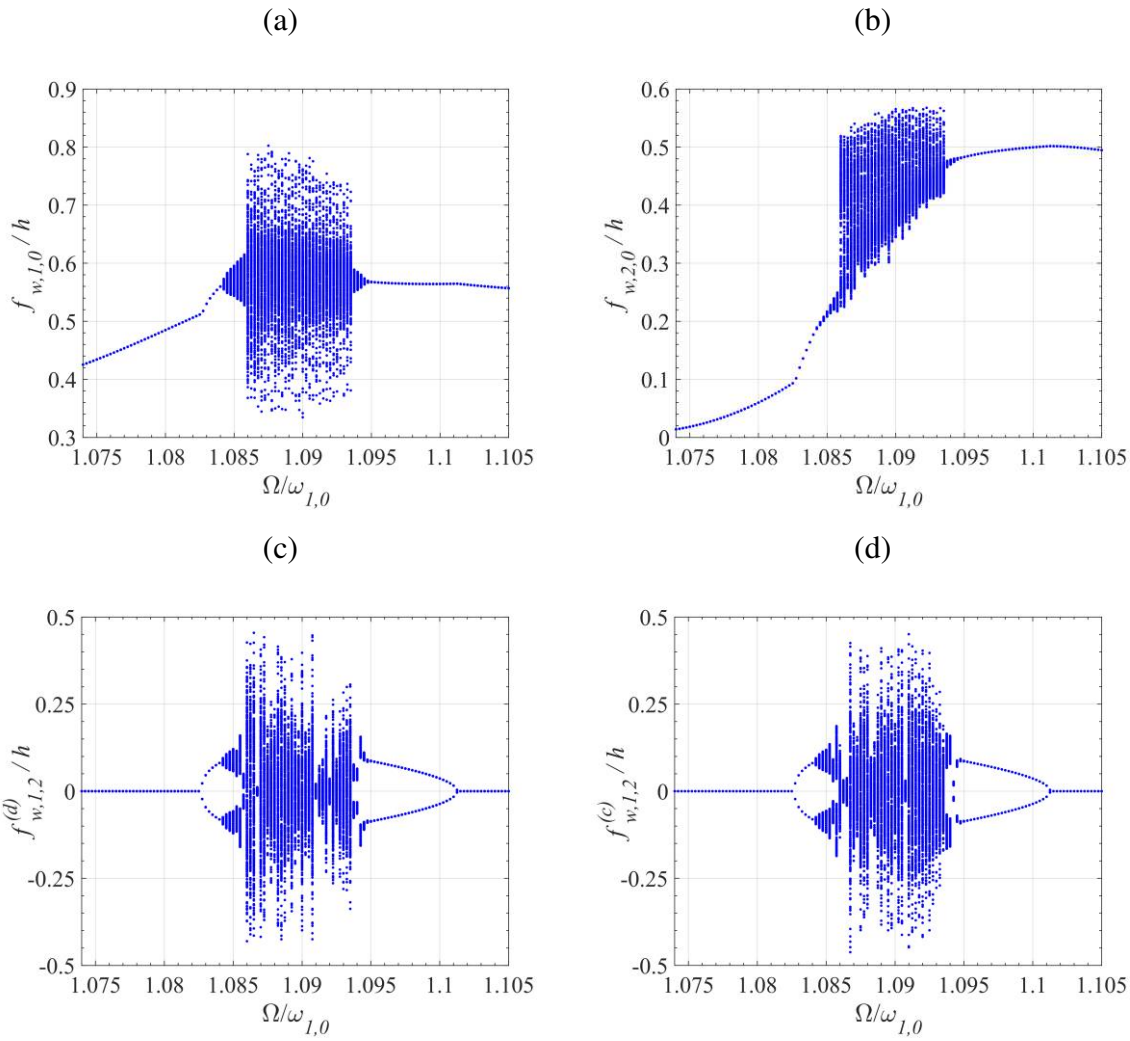

Fig. 3 - Bifurcation diagrams of the Poincaré section for an increasing excitation frequency: (a) first axisymmetric mode, (b) second axisymmetric mode, (c) driven, and (d) companion asymmetric modes (1,2).

From the analysis of the bifurcation diagrams, an interesting phenomenon has been pointed out: for some values of the forcing frequency, axisymmetric vibrations are periodic with the same frequency of the harmonic pressure, while the asymmetric oscillations are 2-T subharmonic. By analyzing the set of the equations, one could see that a coupling between linear terms of the coordinate $f_{w,1,0}$ and $f^{(d)}_{w,1,2}$ is missing in the first equation of the ODEs (when a perfect structure is considered). On the other hand, only odd powers of $f^{(d)}_{w,1,2}$ and products between linear power of $f_{w,1,0}$ and $f^{(d)}_{w,1,2}$ appear in the second equation; therefore, an autoparametric instability takes place when the axisymmetric mode (1,0)

vibrates at the same frequency of the asymmetric mode (1,2), indeed, from Fig.s 3-4, a period-doubling occurs when $\Omega/\omega_{1,0} = 1.10125$, i.e. $\Omega/\omega_{1,2} = 0.9964$.

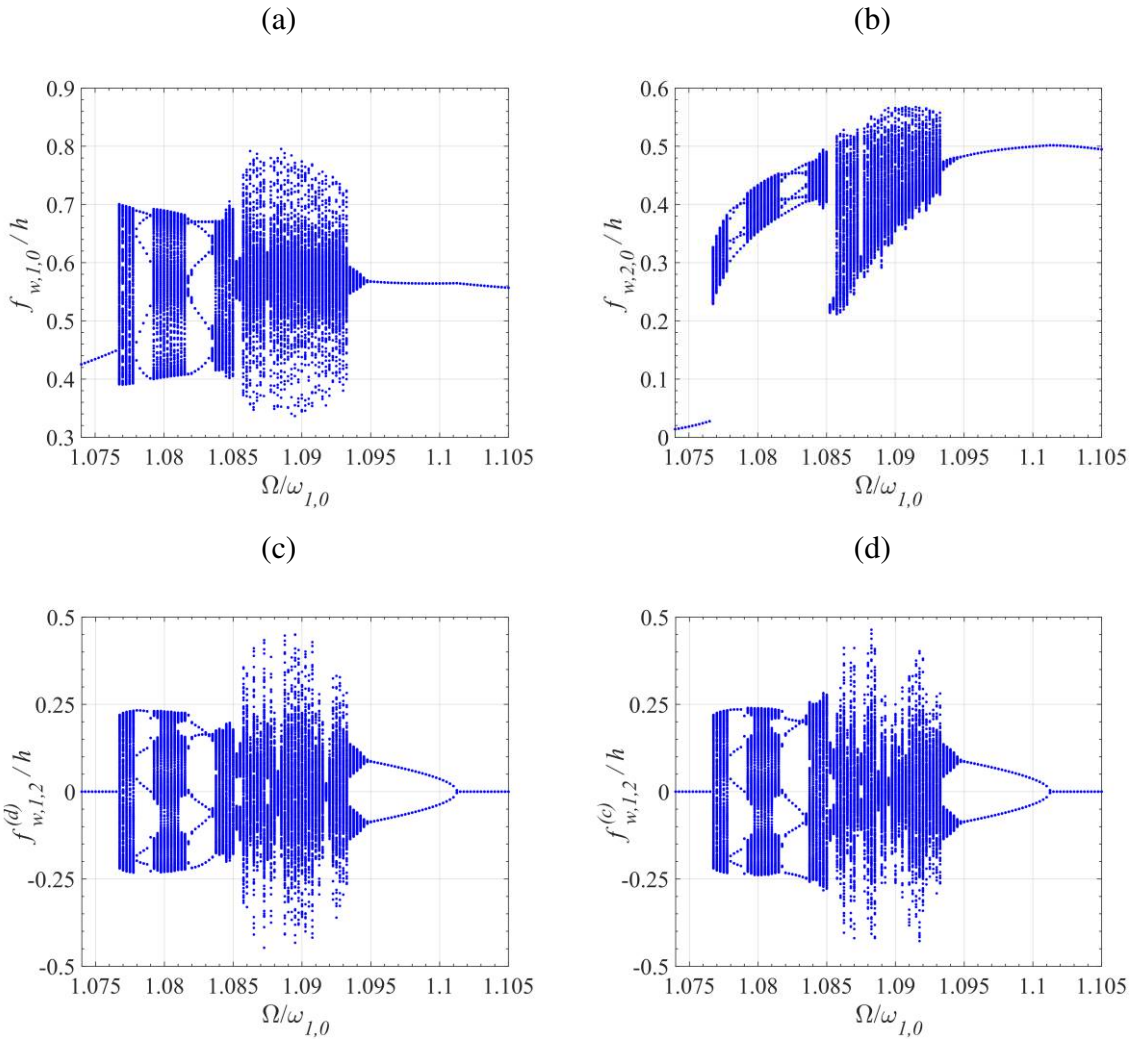

Fig. 4. Bifurcation diagrams of the Poincaré section for a decreasing excitation frequency: (a) first axisymmetric mode, (b) second axisymmetric mode, (c) driven, and (d) companion asymmetric modes (1,2).

As suggested by Moon [47], in order to detect non-periodic or chaotic oscillations it is not sufficient considering only frequency-response or bifurcation diagrams. To this end, other mathematical tools deserve to be simultaneously considered, e.g. time histories, Fourier's spectra, Poincaré sections, and phase portraits.

Without loss of generality, only the case of decreasing excitation frequency is here deeply investigated.

480

(a)

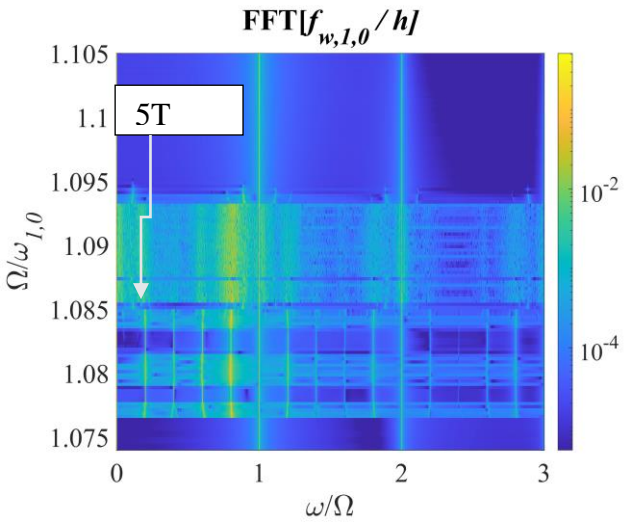

(b)

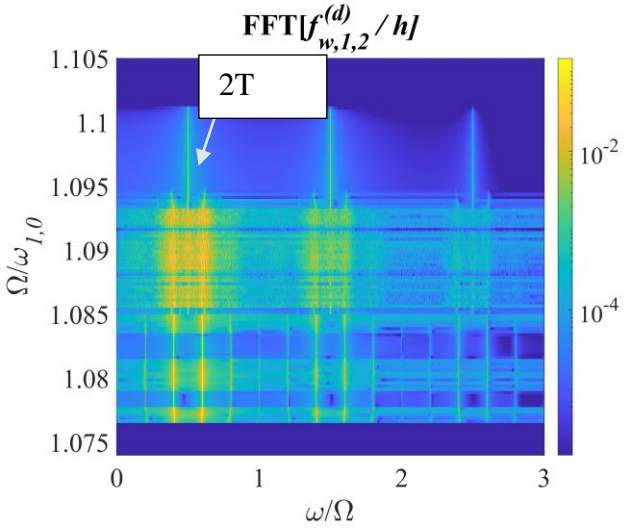

481 **Fig. 5 – Spectrograms of the modal coordinates for a decreasing excitation frequency: (a)**
482 **first axisymmetric mode, (b) driven companion asymmetric modes (1,2).**

483

484 In Fig. 5(a) the spectrogram of $f_{w,1,0}$ is shown. The energy content is localized at
485 the same frequency of the excitation until the instability onset, where the energy
486 spreads on a broad frequency range. On the other hand, the response of the
487 asymmetric mode $f^{(d)}_{w,1,2}$ is mainly ½-subharmonic, see Fig. 5(b). When the
488 frequency of the harmonic pressure is decreasing and crosses $\Omega/\omega_{1,0} = 1.0850$,
489 5T-subharmonic components of the response are clearly visible from both spectra.
490 It is worthwhile to note that in the spectrum of $f^{(d)}_{w,1,2}$ the main 1T-harmonic is
491 almost absent except in the frequency range of strong subharmonic vibrations.

In the following, the development of chaotic oscillations is shown and the behavior of the driven asymmetric mode $f_{w,1,2}^{(d)}$ is deeply addressed to complete the description of the dynamic scenario.

In Fig. 6(a-d) the case $\Omega/\omega_{1,0}=1.0970$ is discussed. The driven asymmetric mode $f_{w,1,2}^{(d)}$ shows a ½-subharmonic: only odd harmonics appear in the spectrum because of the symmetry of the time waveform, Fig. 6(a,b); two points are present in the Poincaré map, Fig. 6(c); the regular limit-cycle shown by the phase portrait confirms the periodicity of the vibration, Fig. 6(d).

$$\Omega/\omega_{1,0}=1.0970$$

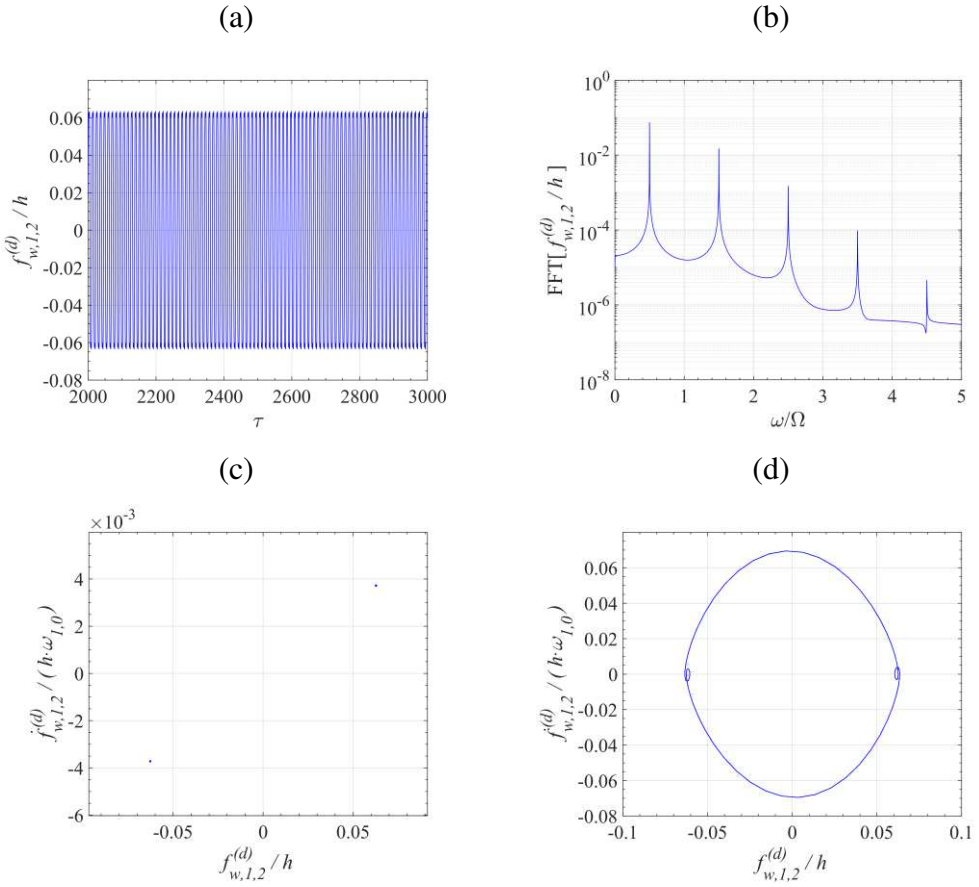

Fig. 6. 2T subharmonic response of the driven modal coordinate (1,2). Decreasing excitation frequency. (a) Time history, (b) Fourier spectrum, (c) Poincaré map, and (d) phase portrait.

The forcing frequency is now reduced to $\Omega/\omega_{1,0}=1.09375$, and the system is in the un-steady region, as depicted in Fig. 4. The Neimark-Sacker bifurcation gives rise to quasi-periodic oscillations, thus the response can be seen as a sum of many periodic functions, where two or more frequencies are incommensurate [48]: in

this case the time response is amplitude-modulated, Fig. 7(a); the carrier frequency is $\omega/\Omega = 1/2$ and sidebands (modulation frequency $\Delta\omega/\Omega = 0.11$) are present, Fig. 7(b); the Poincaré map displays two closed non-connected sets, therefore the response is 2-period quasiperiodic with modulation of the amplitude [49], and the orbit does not close on itself, Fig. 7(c,d).

$$\Omega/\omega_{1,0} = 1.09375$$

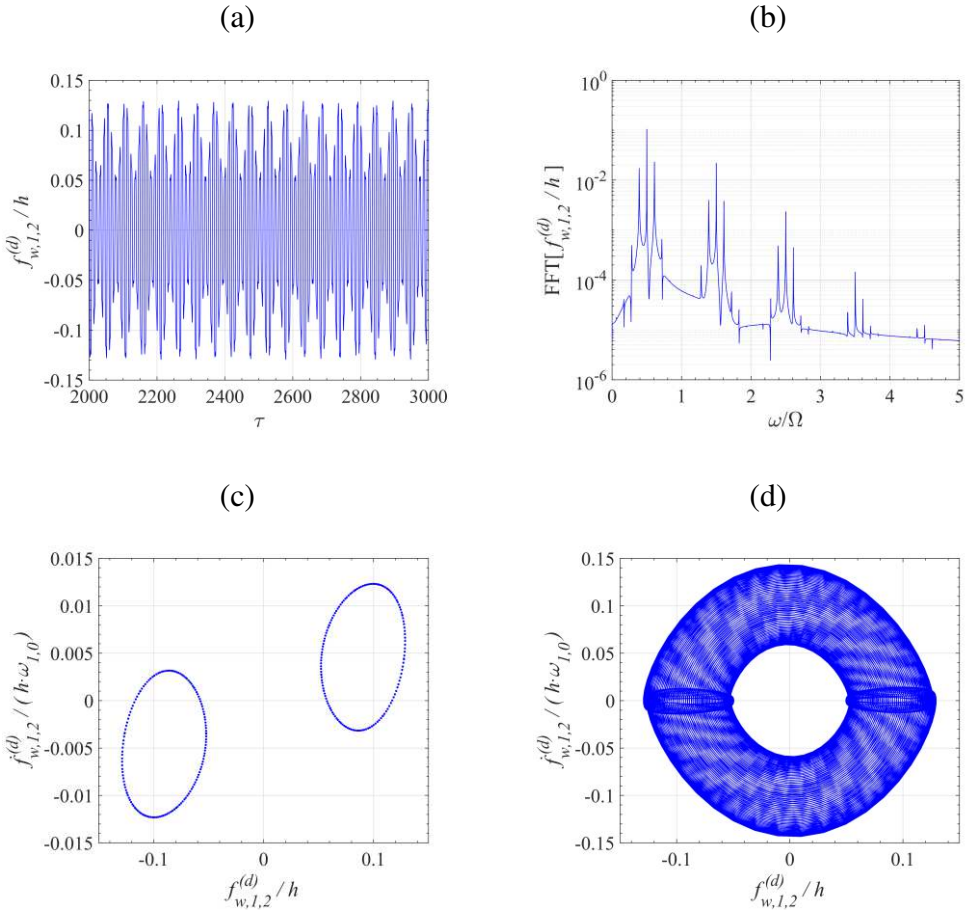

Fig. 7. Amplitude-modulated response of the driven modal coordinate (1,2). Decreasing excitation frequency. (a) Time history, (b) Fourier spectrum, (c) Poincaré map, and (d) phase portrait..

The case at $\Omega/\omega_{1,0}=1.0900$, is now analyzed. Chaotic vibrations can be observed: the time history exhibits intermittency of the response bursts, Fig. 8(a); the spectrum is characterized by a spreading of energy over a broad-band around the carrier frequency (and multiples) $\omega/\Omega=1/2$, Fig. 8(b); the Poincare section shows a set of randomly distributed points, where the dimension of the set does not appear integer, Fig. 8(c), and the trajectory is completely irregular, Fig. 8(d).

$$\Omega/\omega_{1,0}=1.0900$$

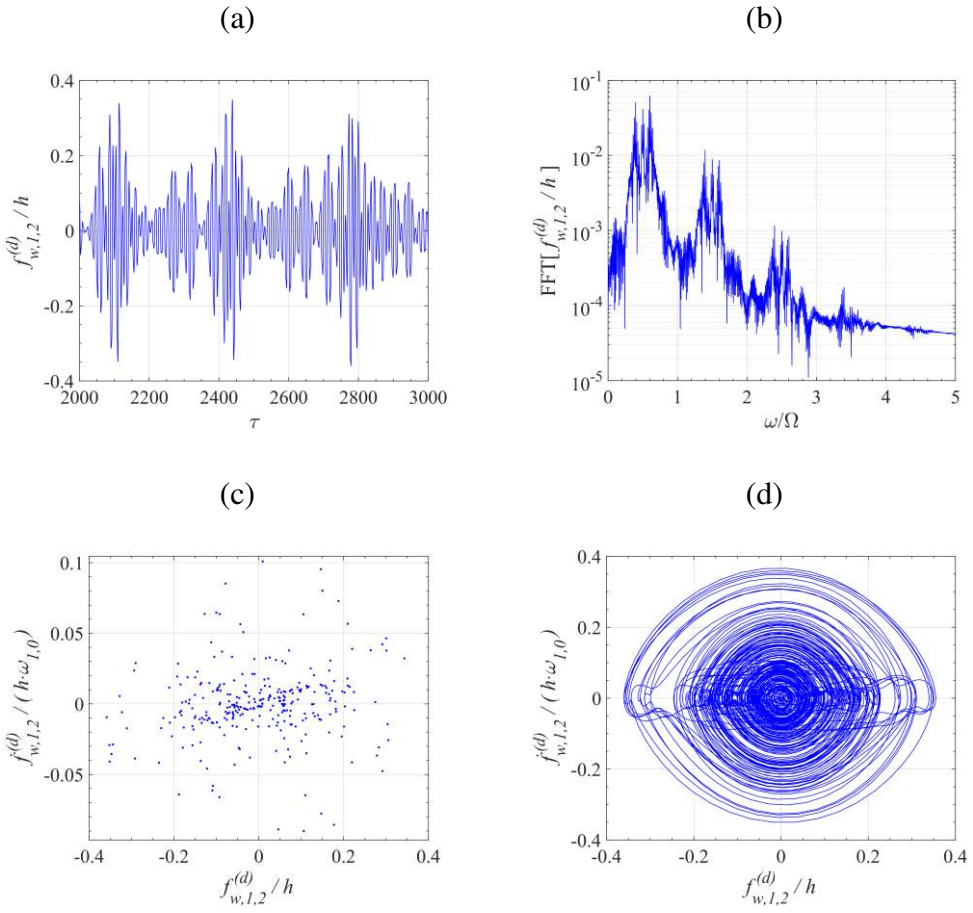

Fig. 8. Chaotic response of the driven modal coordinate (1,2). Decreasing excitation frequency. (a) Time history, (b) Fourier spectrum, (c) Poincaré map, and (d) phase portrait.

Maps of chaotic motion need a larger number of points. Therefore, an additional Poincaré section obtained by considering 10000 forcing periods is shown in Fig. 9. This map clearly shows chaotically modulated oscillations (weak chaos): the central dense pattern is due to the high-frequency vibration, while the outer sparse region is caused by intermittent bursts governed by a slow dynamic. Such set distribution is justified by the Fourier spectrum where, despite its broad energy distribution, the subharmonic components and sidebands give a significant contribution to the overall dynamic of the asymmetric modal coordinate.

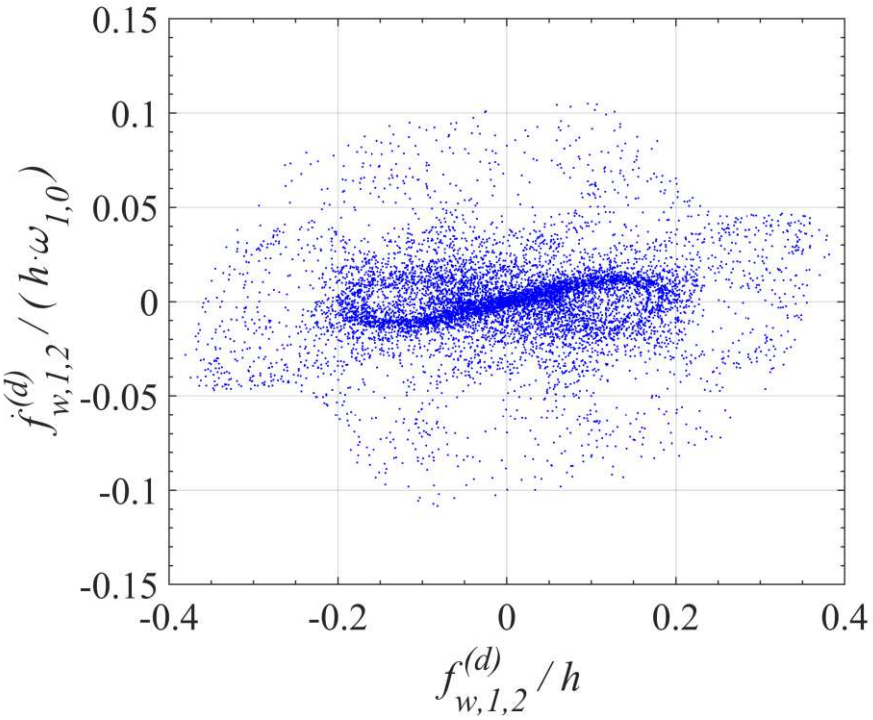

Fig. 9 – Poincaré map of chaotically modulated oscillations.

After a further reduction of the excitation frequency, the system exits form the chaotic region even though it is still inside the "instability region", where an alternance of periodic and non-periodic regions is present. More specifically, the case $\Omega/\omega_{1,0} = 1.0827$ is now analyzed. Here the cap response becomes 5-T subharmonic: the time history appears asymptotically stable, Fig. 10(a); the fundamental frequency is $\omega/\Omega = 1/5$, Fig. 10(b); the Poincaré map shows five dots, Fig. 10(c); the solution follows a closed regular orbit, Fig. 10(d).

549

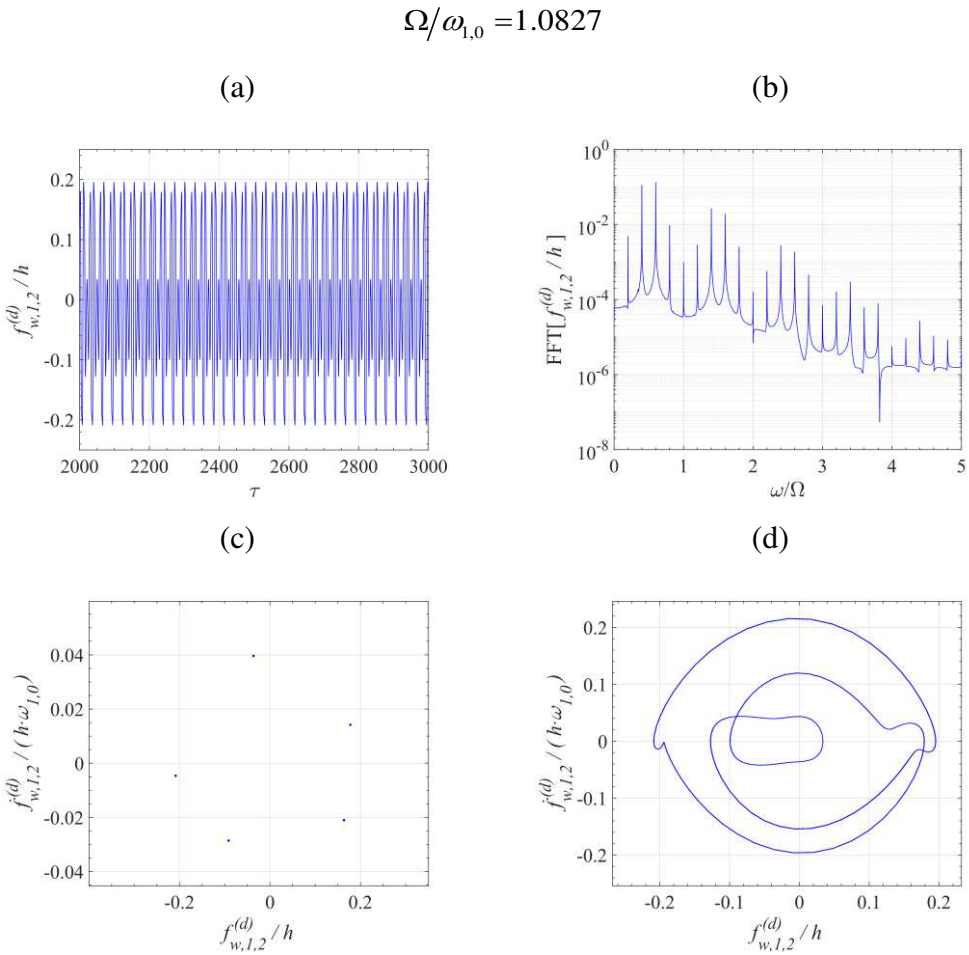

550 **Fig. 10. 5T-subharmonic response of the driven modal coordinate (1,2). Decreasing**
551 **excitation frequency. (a) Time history, (b) Fourier spectrum, (c) Poincaré map, and (d) phase**
552 **portrait.**

553

554 The last case to be investigated is $\Omega/\omega_{1,0}=1.07735$. The coordinate $f^{(d)}_{w,1,2}$ exhibits
555 quasi-periodic oscillations, where the superposition of several periodic functions
556 can be noted by simply observing the time history, Fig. 11(a). The vibration is
557 strongly characterized by a 1/5-subharmonic contribution Fig. 11(b); the phase
558 portrait and the Poincaré section confirms the character of the response, Fig.
559 11(c,d). As already shown by the frequency-response curves and the bifurcation
560 diagrams, a further decrease in the excitation frequency restores a periodic
561 oscillation with a null contribution of the non-symmetric modes.

562

563

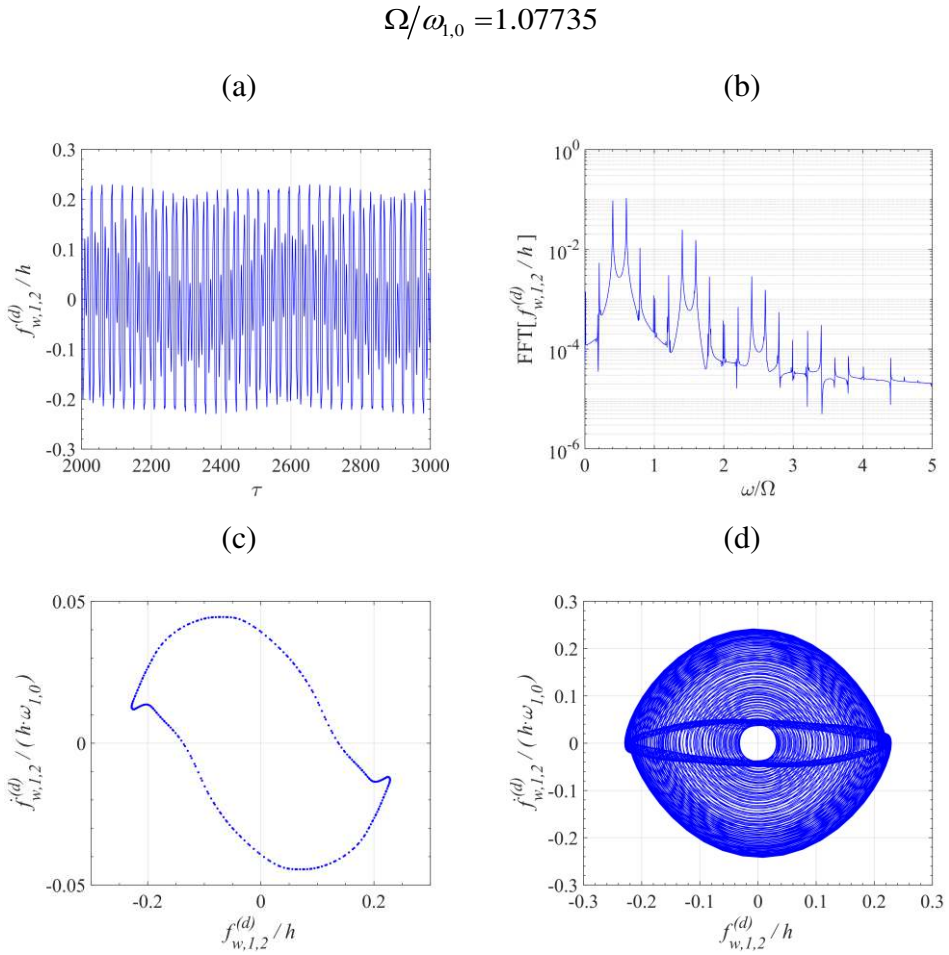

564 **Fig. 11. Quasi-periodic response of the driven modal coordinate (1,2). Decreasing excitation**
565 **frequency. (a) Time history, (b) Fourier spectrum, (c) Poincaré map, and (d) phase portrait..**
566

567 # 4. Conclusions

568 The problem of a shallow spherical cap exhibiting asymmetric oscillations when
569 subjected to a uniform harmonic pressure has been investigated. The
570 Novozhilov's nonlinear shell theory has been considered for defining the strain-
571 displacement relations. The partial differential equations are reduced to a finite
572 dimension by using an energy formulation based on Rayleigh-Ritz approach and
573 Lagrange equations. For describing the cap deformation, the set of displacement
574 field trial functions have been expressed by means of Legendre polynomials and
575 trigonometric functions. A static compressive pressure has been superimposed to
576 a harmonic one. Bifurcation diagrams are investigated against the excitation
577 frequency. The dynamic scenario shows that the spherical cap vibrations turned

out to be often asymmetric, non-periodic, with multiple jumps among subharmonic, quasi-periodic, and chaotic vibrations.

Acknowledgements

The authors acknowledge the University of Modena and Reggio Emilia for supporting this research through the project "Interflu / Non-Newtonian Fluids and Fluid-Structure Interaction".

Funding

FAR2020 Mission Oriented - (CUP E99C20001160007).

Conflict of Interests

The authors declare they have no conflict of interests.

Data availability

Data are available from the authors upon reasonable request.

References

[1] Krenzke, M. A., and Kiernan, T. J., 1963, "Elastic Stability of Near-Perfect Shallow Spherical Shells," AIAA J., **1**(12), pp. 2855–2857.

[2] Huang, N., 1964, "Unsymmetrical Buckling of Thin Shallow Spherical Shells," J. Appl. Mech., **31**(3), pp. 447–457.

[3] Weinitschke, H. J., 1965, "On Asymmetric Buckling of Shallow Spherical Shells," J. Math. Phys., **44**(1–4), pp. 141–163.

[4] Yamada, S., Uchiyama, K., and Yamada, M., 1983, "Experimental Investigation of the Buckling of Shallow Spherical Shells," Int. J. Non. Linear. Mech., **18**(1), pp. 37–54.

[5] Hutchinson, J. W., 1965, *Imperfection-Sensitivity of Externally Pressurized Spherical Shells*, National Aeronautics and Space Administration, NASA-CR-68613.

[6] Gonçalves, P. B., and Croll, J. G. A., 1992, "Axisymmetric Buckling of Pressure-Loaded Spherical Caps," J. Struct. Eng., **118**(4), pp. 970–985.

[7] NASA, 1969, *Buckling of Thin Walled Doubly-Curved Shells*, National Aeronautics and Space Administration, NASA SP-8032.

610 [8] Wagner, H. N. R., Hühne, C., and Niemann, S., 2018, "Robust Knockdown Factors for the
611 Design of Spherical Shells under External Pressure: Development and Validation," Int. J.
612 Mech. Sci., **141**(January), pp. 58–77.
613 [9] Evkin, A. Y., and Lykhachova, O. V, 2019, "Design Buckling Pressure for Thin Spherical
614 Shells: Development and Validation," Int. J. Solids Struct., **156**–**157**, pp. 61–72.
615 [10] Lock, M. H., Okubo, S., and Whittier, J. S., 1968, "Experiments on the Snapping of a
616 Shallow Dome under a Step Pressure Load.," AIAA J., **6**(7), pp. 1320–1326.
617 [11] Stricklin, J. A., Haisler, W. E., Macdougall, H. R., and Stebbins, F. J., 1968, "Nonlinear
618 Analysis of Shells of Revolution by the Matrix Displacement Method.," AIAA J., **6**(12),
619 pp. 2306–2312.
620 [12] Stricklin, J. A., Martinez, J. E., Tillerson, J. R., Hong, J. H., and Haisler, W. E., 1971,
621 "Nonlinear Dynamic Analysis of Shells of Revolution by Matrix Displacement Method,"
622 AIAA J., **9**(4), pp. 629–636.
623 [13] Huang, N. C., 1969, "Axisymmetric Dynamic Snap-through of Elastic Clamped Shallow
624 Spherical Shells.," AIAA J., **7**(2), pp. 215–220.
625 [14] Stephens, W. B., and Fulton, R. E., 1969, "Axisymmetric Static and Dynamic Buckling of
626 Spherical Caps Due to Centrally Distributed Pressures," AIAA J., **7**(11), pp. 2120–2126.
627 [15] Ball, R. E., and Burt, J. A., 1973, "Dynamic Buckling of Shallow Spherical Shells," J.
628 Appl. Mech., **40**(2), pp. 411–416.
629 [16] Akkas, N., 1976, "Bifurcation and Snap-through Phenomena in Asymmetric Dynamic
630 Analysis of Shallow Spherical Shells," Comput. Struct., **6**(3), pp. 241–251.
631 [17] Kao, R., and Perrone, N., 1971, "Asymmetric Buckling of Spherical Caps With
632 Asymmetrical Imperfections," J. Appl. Mech., **38**(1), pp. 172–178.
633 [18] Kao, R., 1980, "Large Deformation Elastic-Plastic Buckling Analysis of Spherical Caps
634 with Initial Imperfections," Comput. Struct., **11**(6), pp. 609–619.
635 [19] Kao, R., 1980, "Nonlinear Dynamic Buckling of Spherical Caps with Initial
636 Imperfections," Comput. Struct., **12**(1), pp. 49–63.
637 [20] Yu, Y. Y., 1964, "Generalized Hamilton's Principle and Variational Equation of Motion in
638 Nonlinear Elasticity Theory, with Application to Plate Theory," J. Acoust. Soc. Am.,
639 **36**(1), pp. 111–120.
640 [21] Grossman, P. L., Koplik, B., and Yu, Y., 1969, "Nonlinear Vibrations of Shallow
641 Spherical Shells," J. Appl. Mech., **36**(3), pp. 451–458.
642 [22] Evensen, H. A., and Evan-Iwanowski, R. M., 1967, "Dynamic Response and Stability of
643 Shallow Spherical Shells Subject to Time-Dependent Loading.," AIAA J., **5**(5), pp. 969–
644 976.
645 [23] Yasuda, K., and Kushida, G., 1984, "Nonlinear Forced Oscillations of a Shallow Spherical
646 Shell," Bull. JSME, **27**(232), pp. 2233–2240.
647 [24] Gonçalves, P. B., 1994, "Axisymmetric Vibrations of Imperfect Shallow Spherical Caps
648 Under Pressure Loading," J. Sound Vib., **174**(2), pp. 249–260.
649 [25] Gonçalves, P. B., 1993, "Jump Phenomena, Bifurcations, and Chaos in a Pressure Loaded
650 Spherical Cap Under Harmonic Excitation," Appl. Mech. Rev., **46**(11S), pp. S279–S288.

[26] Soliman, M. S., and Goncalves, P. B., 2003, “Chaotic Behavior Resulting in Transient and Steady State Instabilities of Pressure-Loaded Shallow Spherical Shells,” J. Sound Vib., **259**(3), pp. 497–512.

[27] Thomas, O., Touzé, C., and Chaigne, A., 2005, “Non-Linear Vibrations of Free-Edge Thin Spherical Shells: Modal Interaction Rules and 1:1:2 Internal Resonance,” Int. J. Solids Struct., **42**(11–12), pp. 3339–3373.

[28] Thomas, O., Touzé, C., and Luminais, É., 2007, “Non-Linear Vibrations of Free-Edge Thin Spherical Shells: Experiments on a 1:1:2 Internal Resonance,” Nonlinear Dyn., **49**(1–2), pp. 259–284.

[29] Touzé, C., and Thomas, O., 2006, “Non-Linear Behaviour of Free-Edge Shallow Spherical Shells: Effect of the Geometry,” Int. J. Non. Linear. Mech., **41**(5), pp. 678–692.

[30] Touzé, C., Thomas, O., and Amabili, M., 2011, “Transition to Chaotic Vibrations for Harmonically Forced Perfect and Imperfect Circular Plates,” Int. J. Non. Linear. Mech., **46**(1), pp. 234–246.

[31] Krysko, V. A., Awrejcewicz, J., Dobriyan, V., Papkova, I. V., and Krysko, V. A., 2019, “Size-Dependent Parameter Cancels Chaotic Vibrations of Flexible Shallow Nano-Shells,” J. Sound Vib., **446**, pp. 374–386.

[32] Iarriccio, G., and Pellicano, F., 2021, “Nonlinear Dynamics and Stability of Shallow Spherical Caps Under Pressure Loading,” J. Comput. Nonlinear Dyn., **16**(2), pp. 1–8.

[33] Novozhilov, V. V., 1953, *Foundations of the Nonlinear Theory of Elasticity*, Graylock Press.

[34] Leissa, A. W., 1973, *Vibration of Shells*, National Aeronautics and Space Administration, NASA SP-288, Washington, D.C.

[35] de Souza, V. C. M., and Croll, J. G. A., 1980, “An Energy Analysis of the Free Vibrations of Isotropic Spherical Shells,” J. Sound Vib., **73**(3), pp. 379–404.

[36] Leissa, A. W., 2005, “The Historical Bases of the Rayleigh and Ritz Methods,” J. Sound Vib., **287**(4–5), pp. 961–978.

[37] Meirovitch, L., 1942, “Fundamentals of Vibration Study,” Nature, **150**(3805), pp. 392–392.

[38] Evensen, D. A., 1966, “Nonlinear Flexural Vibrations of Thin Circular Rings,” J. Appl. Mech., **33**(3), pp. 553–560.

[39] Kubenko, V. D., Koval’chuk, P. S., and Krasnopol’skaya, T. S., 1982, “Effect of Initial Camber on Natural Nonlinear Vibrations of Cylindrical Shells,” Sov. Appl. Mech., **18**(1), pp. 34–39.

[40] Amabili, M., Pellicano, F., and Païdoussis, M. P., 1999, “Non-Linear Dynamics and Stability of Circular Cylindrical Shells Containing Flowing Fluid. Part I: Stability,” J. Sound Vib., **225**(4), pp. 655–699.

[41] Amabili, M., Pellicano, F., and Païdoussis, M. P., 2000, “Non-Linear Dynamics and Stability of Circular Cylindrical Shells Containing Flowing Fluid. Part III: Truncation Effect without Flow and Experiments,” J. Sound Vib., **237**(4), pp. 617–640.

[42] Amabili, M., 2008, *Nonlinear Vibrations and Stability of Shells and Plates*, Cambridge

University Press, Cambridge.

[43] Pellicano, F., 2007, "Vibrations of Circular Cylindrical Shells: Theory and Experiments," J. Sound Vib., **303**(1–2), pp. 154–170.

[44] Amabili, M., and Breslavsky, I. D., 2015, "Displacement Dependent Pressure Load for Finite Deflection of Doubly-Curved Thick Shells and Plates," Int. J. Non. Linear. Mech., **77**, pp. 265–273.

[45] Zoelly, R., 1915, "Uber Ein Knickungsproblem an Der Kugelschale.," ETH Zürich, Zürich, Switzerland.

[46] Hairer, E., and Wanner, G., 1996, *Solving Ordinary Differential Equations II*, Springer, Berlin.

[47] Moon, F. C., 2004, *Chaotic Vibrations : An Introduction for Applied Scientists and Engineers*, Wiley-Interscience, New York.

[48] Parker, T. S., and Chua, L. O., 1987, "Chaos: A Tutorial for Engineers," Proc. IEEE, **75**(8), pp. 982–1008.

[49] Nayfeh, A. H., and Balachandran, B., 1995, *Applied Nonlinear Dynamics*, Wiley, Weinheim.